

SCIENTIFIC REPORTS



OPEN

A reverse micelle strategy for fabricating magnetic lipase-immobilized nanoparticles with robust enzymatic activity

Shixiong Yi¹, Fangyin Dai¹, Cunyi Zhao² & Yang Si²

Enzyme-immobilized nanoparticles that are both catalysis effective and recyclable would have wide applications ranging from bioengineering and food industry to environmental fields; however, creating such materials has proven extremely challenging. Herein, we present a scalable methodology to create *Candida rugosa* lipase-immobilized magnetic nanoparticles (L-MNPs) by the combination of nonionic reverse micelle method and Fe₃O₄ nanoparticles. Our approach causes the naturally abundant and sustainable *Candida rugosa* lipase to ordered-assemble into nanoparticles with high catalytic activity and durability. The resultant L-MNPs exhibit the integrated properties of high porosity, large surface area, fractal dimension, robust enzymatic activity, good durability, and high magnetic saturation (59 emu g⁻¹), which can effectively catalyze pentyl valerate esterification and be easily separated by an external magnet in 60 second. The fabrication of such fascinating L-MNPs may provide new insights for developing functional enzyme-immobilized materials towards various applications.

Enzymes are biocatalysts capable of accelerating a range of chemical transformations relevant to materials production, pharmaceutical development, and renewable energy, which are promising green and sustainable alternative to conventional synthetic strategies¹⁻⁴. In order to adapt to organic reaction media and improve the recovery and reuse efficiency, usually hydrophilic enzymes need to be immobilized on or in specific carriers via physical adsorption or chemical binding⁵⁻⁷. Among the numerous supports investigated and applied for enzyme immobilization, nanomaterials, such as nanoparticles, nanotubes, graphene, and nanowires, combine the robust mechanical strength, high porosity, large surface area, lower mass transfer resistance, and high enzyme loading efficiency, which hold great promise as an exceptional nanoscale carrier for realizing enzyme immobilization⁸⁻¹². However, conventional covalent immobilization of enzymes to nanocarrier was performed in aqueous phase, which was usually associated with a significant activity decrease because the active site might be blocked from substrate accessibility and multiple point-binding^{13,14}. The enzyme could also be denatured due to the random cross-linking between proteins and supports^{14,15}.

Reverse micelles, as the forefront of microemulsion reaction medium, has attracted increasing interesting from the viewpoints of avoidance for the random cross-linking between proteins and supports^{16,17}. The reverse micelles are nano-sized spherical aggregates formed by certain surfactants in non-polar medium spontaneously, which solubilized small amounts of water in their interior so providing a stable aqueous microenvironment, the so-called “water-pool”, in non-aqueous medium¹⁸⁻²⁰. The enzymes could be interfacial-activated for the oil-water interface and tended to localize at the spherical interface with the active sites orientated towards hydrophobic phase owing to a large associated hydrophobic region²¹. These organized enzymes would then form a self-immobilized particle in the presence of cross-linking agents. Several nanocarriers, including carbon nanotubes, copolymer particles, zeolite, and nanoclay, have recently been applied to enzyme immobilization using reverse micelles synthesis²⁰⁻²³. However, previous efforts mainly used these materials as non-functional nanosupports and focused excessively on the loading amount, ignoring the time-consuming and cost enzyme recovery procedures by separation or filtration, which presents major challenges in enzyme immobilization that must be addressed before their extensive practical applications.

¹State Key Laboratory of Silkworm Genome Biology & College of Biotechnology, Southwest University, Chongqing, 400715, P. R. China. ²Fiber and Polymer Science, University of California, Davis, CA, 95616, USA. Correspondence and requests for materials should be addressed to Y.S. (email: ysi@ucdavis.edu)

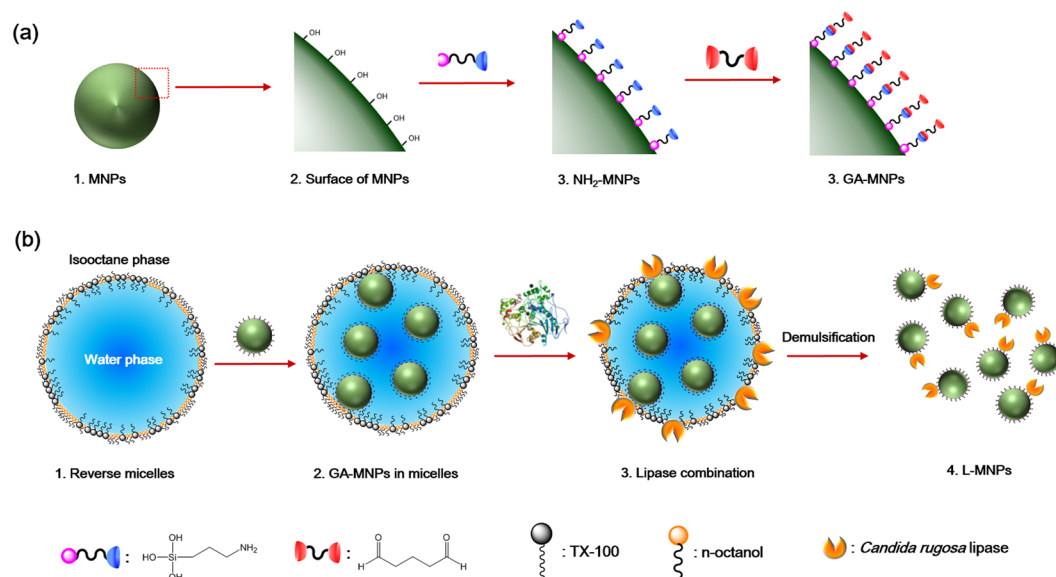


Figure 1. (a) Schematic showing the synthetic steps of the GA-MNPs. (b) Synthesis of L-MNPs through the nonionic reverse micelle method.

Herein, we demonstrate a scalable strategy for creating magnetic lipase-immobilized magnetic nanoparticles (L-MNPs) using a novel nonionic reverse micelle method and Fe₃O₄ nanoparticles. The premise of our design is that the *Candida rugosa* lipase are ordered incorporated into Fe₃O₄ particles with high catalytic efficiency and durability. The L-MNPs exhibited the integrated properties of high porosity, large surface area, robust enzymatic activity, good durability, and easy to magnetic separation, all originating from the synergistic effect of well-organized *Candida rugosa* lipase and magnetic Fe₃O₄ nanoparticles.

Results and Discussion

Reverse Micelle Design: Optimizing Water Polarity. We designed the L-MNPs based on three criteria: (1) the lipase must assemble and bonding to MNPs with a stable covalent linking, (2) the lipase must be exhibit an ordered conformation with high enzymatic bioactivity, and (3) the L-MNPs should be easily collected and separated after reaction. The first two requirements were satisfied by a versatile and readily accessible nonionic reverse micelle method, which allowed quick, easy and reproducible preparation and high structural uniformity of the products. To satisfy the third criterion—we used Fe₃O₄ nanoparticles as magnetic nanocarriers for the ordered loading of lipase. The overall synthesis pathway was schematic showing in Fig. 1. The synthesis process began with the reverse micelles medium by optimizing the water polarity. The magnetic Fe₃O₄ nanoparticles (MNPs) were first modified with free amino groups on the surface (NH₂-MNPs), then bonded with glutaric dialdehyde to form active aldehyde modified MNPs (GA-MNPs). Subsequently, the self-immobilization of lipase on GA-MNPs was carried out in an optimized reverse micelles medium, within vigorously stirring by an ultrasonic mixer. Finally, the lipase modified MNPs (L-MNPs) were facilely separated and collected by an external magnetic field.

It was well known that the ionic systems such as sodium dioctylsulfosuccinate (AOT) reverse micelles would take remarkable influence on enzyme conformation. Usually enzymes showed lower activity compared to that in an aqueous system, which was attributed to the abnormally high polarity of interface regions of the water pool in an ionic surfactant reverse micelle^{24–28}. Therefore, a nonionic reverse micelle system was introduced in this work, and the water polarity was optimized by adjusting the amount of solubilized. The polarity of water in nonionic TX-100 reverse micelles was measured and compared by using ¹H NMR spectra and FT-IR spectra techniques with different *W* values, respectively. Figure 2a and b showed the variation in the NMR chemical shifts of the –OH and –CH₂CH₂O– protons with different *W* values in the TX-100 reverse micelles, respectively. It was observed that the chemical shifts of the –OH moves from about 4.33 to 4.65 ppm with increasing *W* values, while the peak of the proton signal of –CH₂CH₂O– shifts from 3.41 to 3.46 ppm. The chemical shifts variation of the –OH is due to the changes in the environment of the water molecules²⁹. Generally, the hydrogen bonding decreases the electron density around the proton and thus moves the proton absorption to a lower field²⁵. The water molecules are initially tightly bound to the ethylene oxide residues, with a low degree of hydrogen bonding per molecule when the *W* = 1. As the amount of water added in the reverse micelles increased and *W* = 10, the hydration process of the water and ethylene oxide was finished and the free water are formed in this system, which caused the increasing hydrogen bonding. Thus the downfield shift in the –OH signal was produced from 4.33 to 4.65 ppm and the –OH chemical shifts was close to the bulk water value of about 4.79 ppm with increasing *W* values²⁶. In addition, the small change in the –CH₂CH₂O– chemical shift can be ascribed to the changed solvent environment. With the *W* values increased from 1 to 10, the ethylene oxide protons are removed from its initial isooctane environment into the interface of the reverse micelles. Significantly, the ¹H-NMR spectra demonstrated that the polarity of

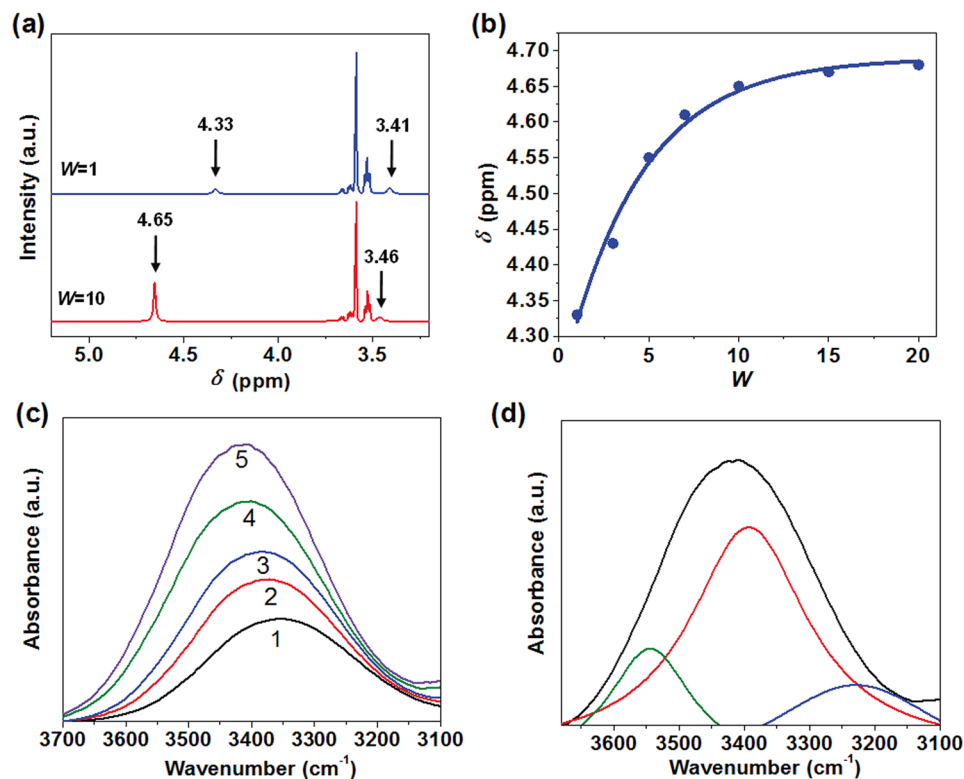


Figure 2. (a) ¹H NMR spectra of TX-100 reverse micelles at $W=1$ and $W=10$. (b) Chemical shift of $-OH$ protons with different W values. (c) FT-IR absorption intensity of $-OH$ stretching vibration with different W values, from samples 1 to 5: $W=0.5, 1.0, 2.0, 5.0,$ and 20 . (d) Curve-fitted for FT-IR peak in water hydroxyl in reverse micelles at $W=20$.

the water added in TX-100 reverse micelles increased with increasing W values and get closer to the bulk water, which is of great importance to achieve well enzyme conformation with promising enzymatic activity^{30–33}.

This result was further confirmed by FT-IR analysis, as shown in Fig. 2c and d. The total peak area of $-OH$ stretching band of water solubilized in TX-100 reverse micelles changed with different W values. The variation of $-OH$ stretching frequencies of water as a function of W in this system, where the $-OH$ stretching vibration of water molecules shift from 3348 to 3410 cm^{-1} . This is similar to the variation of $-OH$ stretching frequency of water with increasing W in the water/AOT/*n*-heptane system. The $-OH$ stretching frequency of 3410 cm^{-1} is the same as that of bulk water. Thus, it was concluded that the water solubilized in reverse micelles behaves analogous the bulk water with increasing W values. When the amount of water was small in the reverse micelles, the polarity of water was lower than that in bulk water. It was believed that the polarity of water solubilized in TX-100 reverse micelles at higher W values was similar to that in bulk water. The activities of lipase could be remained in TX-100 reverse micelles.

Morphology and Structure of L-MNPs. It was shown from Fig. 3a and b that the L-MNPs before and after immobilization was with narrow size distribution by TEM observation. This revealed that the conjugation process did not significantly result in agglomeration and change in size of the nanoparticles, which could be attributed to the fact that the reaction occurred only on the Fe_3O_4 nanoparticle surface³⁴. Fig. 3c indicated the mean particle diameter of the L-MNPs before and after immobilization was about 25 nm, and most of the L-MNPs had particle sizes of 30 – 35 nm, which matched well with the TEM results. Moreover, the AFM image also indicated that the preference for particles to self-associate, probably due to magnetic attraction, the absence of a strong interaction with the substrate, and the procedure of sample preparation (Fig. 3d). It is not possible to recognize discrete single enzyme nanoparticle moieties because of the aggregation between particles.

To provide insight into the nanoporous structure, we investigated the effect of lipase immobilization on the rough structure of resultant MNPs through N_2 adsorption at 77 K. As shown in Fig. 4a, the curves exhibited the isotherm of type IV with a series of typical adsorption behaviours including monolayer adsorption, multilayer adsorption and capillary condensation, indicating the characteristics of mesopores within the as-prepared membranes^{35, 36}. And the hysteresis between adsorption and desorption isotherms reveal that the relevant mesopores are open, thus it cause the difference of capillary force for N_2 adsorption and desorption. The narrow H_3 hysteresis loop during the high pressure regimes revealed that the mesopores are conform and open, within no significant interruption between the capillary evaporation and condensation for N_2 ³⁶. The relevant Brunauer-Emmett-Teller (BET) surface area of initial GA-MNPs and L-MNPs were 42.14 and 37.52 m^2 g^{-1} , respectively. The slight decrease of surface area after immobilization was due to the increase of particle size.

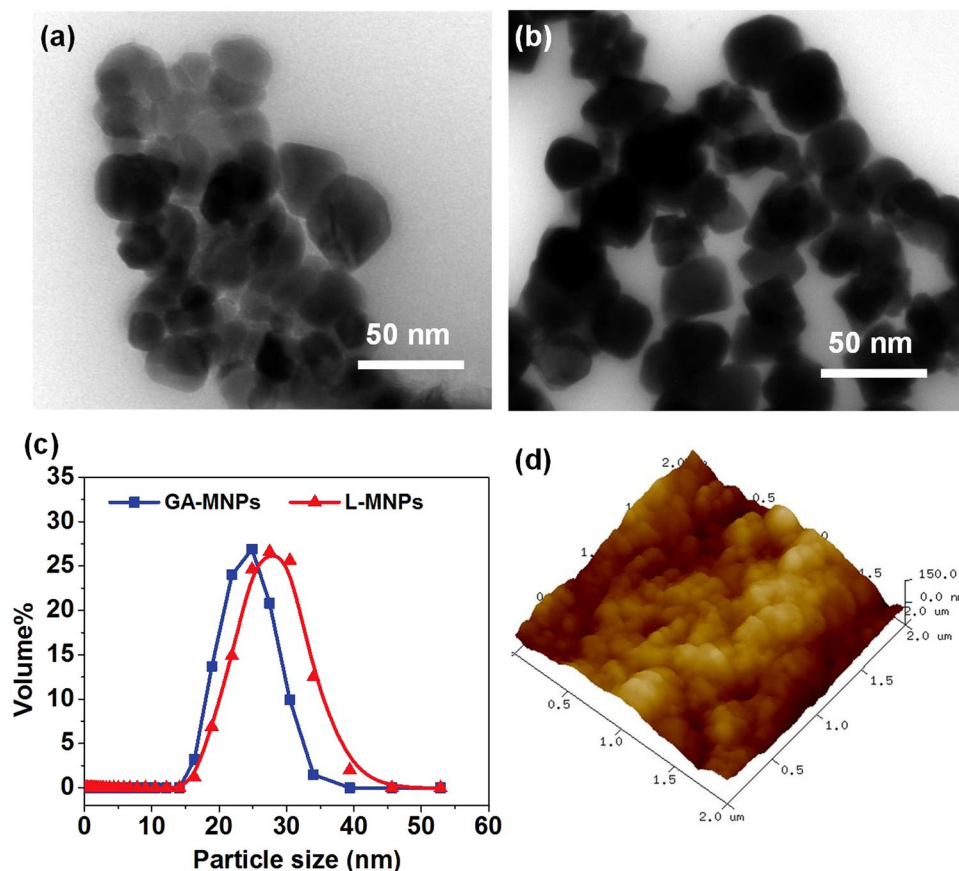


Figure 3. TEM images of (a) GA-MNPs and (b) L-MNPs. (c) Particle size distribution curves of GA-MNPs and L-MNPs. (d) AFM topographic image of the L-MNPs in an small area of $2 \times 2 \mu\text{m}^2$.

The fascinating adsorption isotherms of as-prepared L-MNPs enabled us to deeply investigate their hierarchical rough structure. The immobilization induced structural reorganization was investigated by quantitatively fractal analysis. Fractal dimension (D) with the values of 2 and 3 described a perfectly flat and a totally irregular rough surface, respectively, and hence, the fractal information determined for MNP samples indicated the hierarchical surface roughness. The calculation of D was through the modified Frenkel-Halsey-Hill (FHH) theory of multilayer gas adsorption:^{36,37}

$$\ln(V/V_{\text{mono}}) = A[\ln(\ln(p_0/p))] + \text{constant} \quad (1)$$

where, V is the amount of N_2 adsorbed at each equilibrium pressure, V_{mono} is the amount adsorbed of monolayer coverage (calculated through the BET equation), and p_0 is the saturation pressure. Thus, a plot of $\ln(V/V_{\text{mono}})$ versus $\ln(\ln(p_0/p))$ displayed a linear character, and the slope A could be used to calculate D utilizing the expression: $D = A + 3$, which was according to the dominant forces of liquid-gas surface tension at high coverage^{38,39}. Fig. 4b presented the relevant FHH plots reconstructed from N_2 adsorption isotherms, indicating two distinct linear regions according to monolayer and high coverage regions. Because the interface of mesopore adsorption and capillary condensation is controlled by the liquid-gas surface tension forces, the slopes over the high coverage regions were taken to ensure a reliable evaluation of D ^{39,40}. The resultant D values of GA-MNPs and L-MNPs were 2.796 and 2.672, respectively, revealing the typical surface fractal feature with irregular rough structure. It is noteworthy that the L-MNPs retained over 95% of the original D values after immobilization, indicating a highly rough surface which is of great importance for effective catalysis.

In order to prove the nanoparticles are Fe_3O_4 with comparatively high purity, the XRD pattern of GA-MNPs and L-MNPs were measured and compared, respectively. Figure 4c presented the diffraction peaks of L-MNPs from (220), (311), (400), (422), (511) and (440) are respectively observed at $2\theta = 30.123^\circ$, 35.499° , 43.122° , 53.483° , 57.040° , 62.621° , while the corresponding peaks of GA-MNPs appear at $2\theta = 30.081^\circ$, 35.442° , 43.119° , 53.418° , 57.000° , and 62.581° . These results corresponded to the standard diffraction spectra (JCPDS: 65-3107), which suggested that MNPs is Fe_3O_4 with comparatively high purity, and the conjugation process of L-MNPs derived from GA-MNPs in TX-100 reverse micelles does not result in the phase change of Fe_3O_4 nanoparticles⁴¹.

The FT-IR spectra of L-MNPs obtained in TX-100 reverse micelles were measured at various stages of immobilization. For the three particles, the strong absorption band around 580 cm^{-1} was ascribed to the Fe-O bond of Fe_3O_4 , while the band around 3445 cm^{-1} was assigned to the stretching and bending vibrations of hydroxyl groups. It was seen from NH_2 -MNPs curve that the new peaks at 1111 cm^{-1} and 1026 cm^{-1} referring to stretching

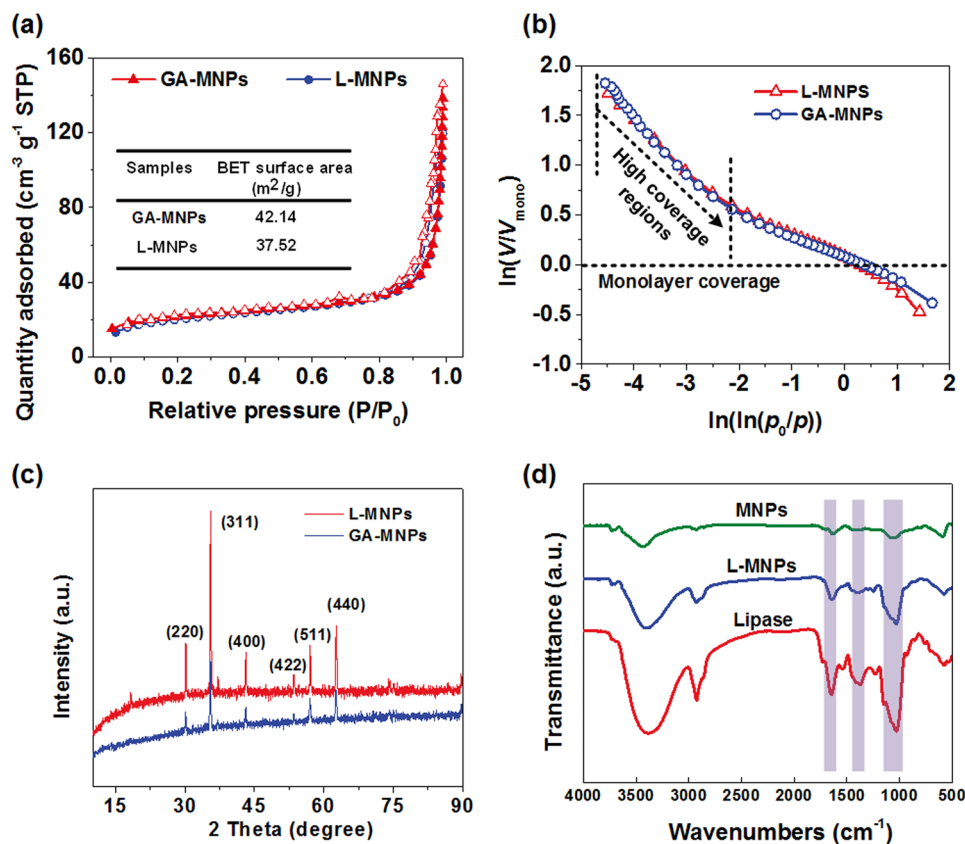


Figure 4. (a) N₂ adsorption–desorption isotherms of L-MNPs before and after immobilization. (b) FHH plots of $\ln(V/V_{\text{mono}})$ against $\ln(\ln(p_0/p))$ reconstructed from the relevant N₂ adsorption isotherms. (c) The XRD patterns of GA-MNPs and L-MNPs. (d) FT-IR spectra of MNPs, L-MNPs and *Candida rugosa* lipase.

vibration of Si–O, which might give evidence of the existence of APTES (Figure S1). In addition, it was showed from Fig. 4d that the strong absorption peak of L-MNPs in the 1700–1600 cm⁻¹ region, 1580–1510 cm⁻¹ region, 1400–1200 cm⁻¹ region and 1200–900 cm⁻¹ region corresponded to the C=O stretching vibrations, N–H bending, C–N stretching vibrations and protein-associated sugar chains, respectively⁴². The characteristic adsorption bands were similar to that of *Candida rugosa* lipase, which confirmed the conjugation of lipase on GA-MNPs in TX-100 reverse micelles.

Catalytic Performance for Esterification. The uniform and small sizes of the magnetic nanoparticles provided them with a high surface area-to-volume ratio, large density of binding sites for immobilization of enzyme, excellent dispersibility in water, fast motion with agitation, and rapid response toward magnetic field, which is of interest to their catalytic performance. As shown in Fig. 5a, in contrast to the poor activity of L-MNPs synthesis from common water system, the as-prepared L-MNPs from reverse micelle systems exhibit similar enzymatic activity with free *Candida rugosa* lipase, only slight decrease in catalytic efficiency was observed, highlighting the robust immobilization structure. Further quantitative relationship between the synthetic rate and the reaction time (t) for different *Candida rugosa* lipase was analyzed. A pseudo-first-order kinetic model was employed to fit the experimental data. The rate constant is defined as the slope of the plot for the equation for the first-order reaction^{43,44}.

$$\ln(1 - C_t/C_e) = -k_1 t \quad (2)$$

where k_1 is the rate constant and t is the reaction time (min), C_t and C_e are the synthetic rate of pentyl valerate at a time (t) and at equilibrium, respectively.

Figure 5b and Table 1 indicated that the synthetic process of pentyl valerate could be described by using a pseudo-first-order kinetic equation. The k obtained for L-MNPs synthesis from reverse micelles retained over 70% of the original enzymatic activity comparing with free *Candida rugosa* lipase, which was also increased over 150% than that of L-MNPs synthesis from common water system, demonstration the promising immobilization efficiency. This result was contributed by effective binding of enzyme molecules via hydrophobic interactions involving the active site which lead to a nonactive conformational change in enzyme structure or by spreading of enzyme on the Fe₃O₄ particles surface leading to an inactive configuration. Although immobilization of enzymes generally enhance their stability in bulk water, one major disadvantage of random immobilization of enzymes onto nanoparticles is that the activity of the immobilized enzyme is often significantly decreased because the

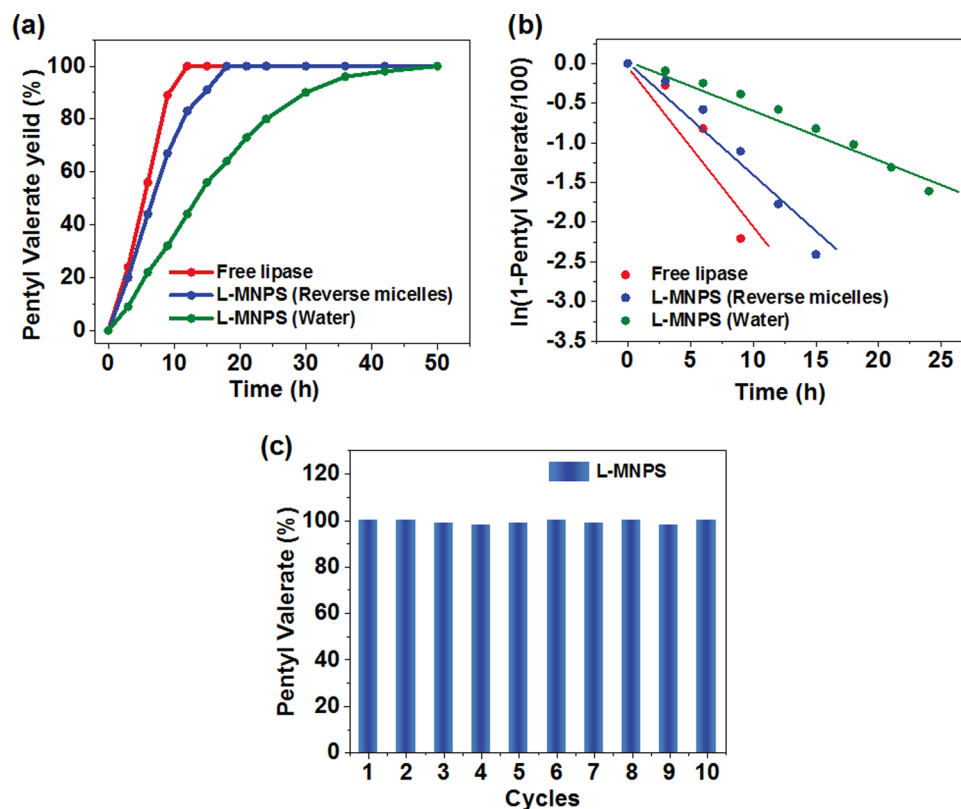


Figure 5. (a) Synthesis of pentyl valerate in cyclohexane using L-MNPs (synthesis from reverse micelles), L-MNPs (synthesis from water), and free *Candida rugosa* lipase. (b) The pseudo-first-order kinetic plot for synthesis of pentyl valerate for relevant samples. (c) Reversibility of the catalytic capacity for L-MNPs over 10 cycles.

Samples	k_1	R
Free lipase	0.2389	0.9421
L-MNPs (from reverse micelles)	0.1695	0.9844
L-MNPs (from water)	0.0670	0.9764

Table 1. Results from linear regression of the plots for the pseudo-first-order kinetic equation.

active site may be blocked from substrate accessibility, multiple point-binding may occur, or the enzyme may be denatured. The nonionic reverse micelles were prepared and used as reaction medium for immobilization of *Candida rugosa* lipase, which avoid the random cross-linking between proteins and supports. Thus, the catalytic properties were improved. In order to evaluate the economic plausibility, it is very important for us to study the reusability of L-MNPs. We performed the reusability of L-MNPs for 10 times, and the influence of repetitive usage on catalytic capacity for synthesis of pentyl valerate was investigated. It was seen from Fig. 5c that the relatively stable catalytic capacity of L-MNPs was nearly constant even after being reused for 10 cycles, indicating the robust durability for long-term using.

Magnetic Separation Performance. Figure 6a displayed the hysteresis loops of GA-MNPs and L-MNPs, which indicates they possess the magnetic saturation (MS) values of 65 emu g^{-1} and 59 emu g^{-1} , respectively. It was worth noting that the remanence of these nanoparticles is zero once the applied magnetic field is removed, implying that these nanoparticles are superparamagnetic⁴⁵. The superparamagnetic properties of the magnetic nanoparticles is critical for their application in biomedical and bioengineering field, which prevents them from aggregation and enables them to redisperse rapidly when the magnetic field is removed. These magnetically active properties of the L-MNPs render them very susceptible to magnetic fields and therefore make the solid L-MNPs and liquid phases separate easily without tedious separation processes (Fig. 6b), which is of great importance for real applications.

Conclusions

In summary, we have presented scalable, synergistic assembly strategy for fabricating magnetic, hierarchical-structured L-MNPs by the combination of nonionic reverse micelle method and Fe_3O_4 nanoparticles.

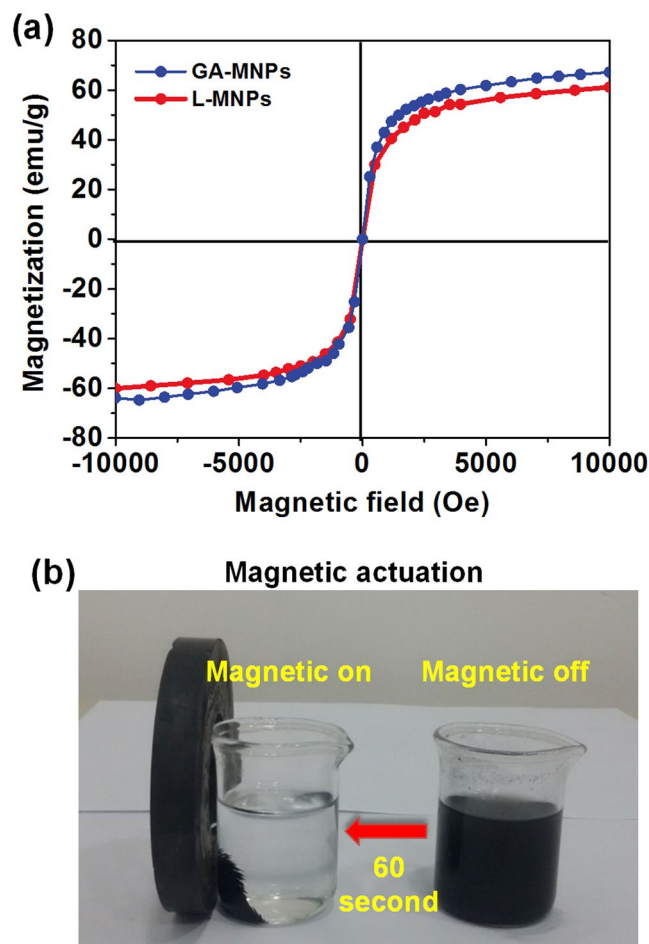


Figure 6. (a) The hysteresis loops of L-MNPs before and after immobilization. GA-MNPs. (b) Photograph showing the fast magnetic responsive performance of L-MNPs after catalytic reaction.

For the first time, the naturally abundant *Candida rugosa* lipase was ordered-assemble into nanoparticles with high catalytic activity and durability. Benefiting from the high porosity, large surface area, fractal dimension, robust enzymatic activity, good durability, and high magnetic saturation (59 emu g^{-1}), the L-MNPs effectively catalyze pentyl valerate esterification in a fast speed and facily separated by an external magnet in 60 second. We expect that such fascinating L-MNPs will open up numerous opportunities for a wide range of applications in future industrial applications such as synthesis of biocatalysis, biomedical diagnostics, biosensors, microfluidics cells, and wastewater treatment.

Experimental Section

Materials and Reagents. Polyoxyethylene tert-octylphenyl ether (TX-100), n-octanol, isooctane, glutaric dialdehyde, 3-Aminopropyl triethoxysilane (APTES), 1-pentanol, and valeric acid were supplied by Chongqing Taixin Chemical Reagent Co. Ltd, China. Fe_3O_4 magnetic nanoparticles (MNPs, 15~30 nm) were supplied from Aladdin Chemical Co. Ltd, China. *Candida rugosa* lipase (type VII) was purchased from Sigma-Aldrich, St. Louis, MO, USA. Pure water with a resistance of 18.2 M Ω was obtained from a Millipore system.

Preparation of Reverse Micelles. TX-100 and n-octanol with a 1:6 molar ratio were dissolved in isooctane at room temperature (TX-100 concentration of 0.2 mol L^{-1}), and then a given volume of aqueous solution was dropped into the mixture using a microsyringe. After the injection, the mixture was vigorously stirred and treated using an ultrasonic mixer until it became a transparent reverse micelle system. The quantity of solubilized aqueous solution in the reverse micelle was shown by the molar ratio (W) of injected aqueous solution to TX-100, that is, $W = [\text{H}_2\text{O}]/[\text{TX}-100]$ ^{46, 47}. The structure of TX-100 reverse micelle was shown in Fig. 1.

Fabrication of Glutaric Dialdehyde Modified MNPs. Figure 1a Describes the synthesis pathway. Generally, the MNPs were put in a mixture of 75 mL of water and 50 mL of ethanol. In order to disperse completely, the mixed solution was ultrasonically agitated for 0.5 h. After that, a certain amount of APTES was added. Then the mixture solution was kept stirring for 40 h before separation. The MNPs modified with APTES (NH_2 -MNPs) were prepared and washed with ethanol for 5 times. Subsequently, the NH_2 -MNPs was added in the 20 mL ethanol, then mixed with 25 mL glutaric dialdehyde (25%) and kept at 200 °C for 10 h with continuous

agitation (200 rps). Finally, the NH₂-MNPs activated with glutaric dialdehyde (GA-MNPs) were and obtained and washed with ethanol and water for 4 times, respectively.

Immobilization of Lipase on GA-MNPs. As shown in Fig. 1b, the immobilization of lipase on GA-MNPs was carried out in TX-100 reverse micelles. 50 μL of *Candida rugosa* lipase solution (3 mg mL⁻¹) was mixed with 50 μL of GA-MNPs solution. The mixed aqueous solution was added in the 50 mL of TX-100 reverse micelles ($W = 10$). Thereafter, the mixture was vigorously stirred and treated using an ultrasonic mixer until it became a transparent reverse micelle system. Finally, the L-MNPs were obtained and separated by an external magnetic field. For comparison with traditional synthesis method using water reaction medium, the 50 μL of lipase solution (3 mg mL⁻¹) and 50 μL of GA-MNPs solution were added in 5 mL of Tris-HCl buffer (pH = 8.5). The mixture was shaken at 30 °C for 2 h. Finally, the L-MNPs were obtained and separated by an external magnetic field.

Measurement of the Catalytic Performance. The catalytic performance of L-MNPs obtained in reverse micelles and in bulk water were tested for synthesis of pentyl valerate. After immobilization, the reaction system consisted of 2 mL of cyclohexane supplemented with equimolar (100 mM) concentrations each of 1-pentanol and valeric acid in 10 mL screw capped bottles. The reaction was initiated by addition of L-MNPs and shaking at 37 °C and 200 rpm in an orbital shaker. Esterification reaction using free enzyme equivalent to the amount immobilized on MNPs was also performed. The samples were withdrawn at regular intervals and the quantification of accumulated ester was analyzed on Agilent Technologies 6890 N network GC systems, USA, with a flame ionization detector²¹.

Characterization. ¹H NMR spectra of TX-100 reverse micelles with different W values was conducted on an Inava 500MHz NMR spectrometer (Varian Corporation, USA). FT-IR spectra of the water existed in reverse micelles with different W values was recorded over the range of 1000–4000 cm⁻¹ with a Nicolet 8700 FT-IR spectrometer. The particle size distribution of the L-MNPs was determined with Particle Size Analyzer (DelsaTM Nano C Beckman Coulter, USA). The Brunauer–Emmet–Teller (BET) surface area was characterized using N₂ adsorption–desorption isotherms with a surface area analyzer (ASAP 2020, micromeritics Co., USA). The morphology and structure of the L-MNPs were observed using transmission electron micrograph (TEM) with 120 kV (JEM-1200EX). The crystalline state of the L-MNPs was measured by X-ray diffractometer (Ultima IV; Rigaku, Tokyo, Japan). The imaging of L-MNPs for AFM was performed using a Nanoscope Multimode Scanning Probe Microscope equipped with an EV scanner operating in tapping mode. The magnetic measurements were carried out with a superconducting quantum interference device model MPMS XI-7 magnetometer (USA) at a maximum magnetic field of 7 T and a sensibility of 10⁻⁶ emu.

References

- Matsumura, S., Soeda, Y. & Toshima, K. Perspectives for synthesis and production of polyurethanes and related polymers by enzymes directed toward green and sustainable chemistry. *Appl. Microbiol. Biot.* **70**, 12–20 (2006).
- Shoda, S., Uyama, H., Kadokawa, J., Kimura, S. & Kobayashi, S. Enzymes as green catalysts for precision macromolecular synthesis. *Chem. Rev.* **116**, 2307–2413 (2016).
- Wang, M. *et al.* A green approach to the synthesis of novel “Desert rose stone”-like nanobiocatalytic system with excellent enzyme activity and stability. *Sci. Rep.* **4**, 6606 (2014).
- Wang, X. D., Rabe, K. S., Ahmed, I. & Niemeyer, C. M. Multifunctional silica nanoparticles for covalent immobilization of highly sensitive proteins. *Adv. Mater.* **27**, 7945–7950 (2015).
- Correro, M. R. *et al.* Enzyme shielding in an enzyme-thin and soft organosilicalayer. *Angew. Chem. Int. Ed.* **55**, 6285–6289 (2016).
- Si, Y., Yu, J. Y., Tang, X. M., Ge, J. L. & Ding, B. Ultralight nanofibre-assembled cellular aerogels with superelasticity and multifunctionality. *Nat. Commun.* **5**, 5802 (2014).
- Tang, X. M. *et al.* *In situ* polymerized superhydrophobic and superoleophilic nanofibrous membranes for gravity driven oil-water separation. *Nanoscale* **5**, 11657–11664 (2013).
- Torres-Salas, P. *et al.* Immobilized biocatalysts: novel approaches and tools for binding enzymes to supports. *Adv. Mater.* **23**, 5275–5282 (2011).
- Kuang, W. *et al.* Investigation of internal concentration polarization reduction in forward osmosis membrane using nano-CaCO₃ particles as sacrificial component. *J. Membr. Sci.* **497**, 485–493 (2016).
- Sun, H., Schiraldi, D. A., Chen, D. Y., Wang, D. Q. & Sanchez-Soto, M. Tough polymer aerogels incorporating a conformal inorganic coating for low flammability and durable hydrophobicity. *ACS Appl. Mater. Inter.* **8**, 13051–13057 (2016).
- Pogorilyi, R. P., Melnyk, I. V., Zub, Y. L., Seisenbaeva, G. A. & Kessler, V. G. Enzyme immobilization on a nanoadsorbent for improved stability against heavy metal poisoning. *Colloids Surf. B* **144**, 135–142 (2016).
- Zhang, Y. *et al.* An emerging dual collaborative strategy for high-performance tumor therapy with mesoporous silica nanotubes loaded with Mn₃O₄. *J. Mater. Chem. B* **4**, 7406–7414 (2016).
- Samanta, B. *et al.* Catalytic microcapsules assembled from enzyme-nanoparticle conjugates at oil-water interfaces. *Angew. Chem. Int. Ed.* **48**, 5341–5344 (2009).
- Voelker, A. E. & Viswanathan, R. Self-catalyzed immobilization of gst-fusion proteins for genome-encoded biochips. *Bioconjugate Chem.* **24**, 1295–1301 (2013).
- Mohammadi, M. *et al.* Improvement of the stability and selectivity of Rhizomucor miehei lipase immobilized on silica nanoparticles: Selective hydrolysis of fish oil using immobilized preparations. *Process. Biochem.* **49**, 1314–1323 (2014).
- Liu, T., Zhao, Y. D., Wang, X. F., Li, X. & Yan, Y. J. A novel oriented immobilized lipase on magnetic nanoparticles in reverse micelles system and its application in the enrichment of polyunsaturated fatty acids. *Bioresour. Technol.* **132**, 99–102 (2013).
- Raghavendra, T., Vahora, U., Shah, A. R. & Madamwar, D. Enhanced conjugation of candida rugosa lipase onto multiwalled carbon nanotubes using reverse micelles as attachment medium and application in nonaqueous biocatalysis. *Biotechnol. Progr.* **30**, 828–836 (2014).
- Yi, S. X., Tong, X. L., Sun, S. & Dai, F. Y. Dyeing properties of CI reactive violet 2 on cotton fabric in non-ionic TX-100/Span40 mixed reverse micelles. *Fiber Polym.* **16**, 1663–1670 (2015).
- Seelan, S., Sinha, A. K., Kato, K. & Yokogawa, Y. Enhanced aldol reaction using an aldolase I antibody immobilized in 3D mesoporous silica foam. *Adv. Mater.* **18**, 3001–3004 (2006).
- Yi, S. X. *et al.* Adsorption and fixation behaviour of CI Reactive Red 195 on cotton woven fabric in a nonionic surfactant Triton X-100 reverse micelle. *Color. Technol.* **128**, 306–314 (2012).

21. Solanki, K. & Gupta, M. N. Simultaneous purification and immobilization of *Candida rugosa* lipase on superparamagnetic Fe₃O₄ nanoparticles for catalyzing transesterification reactions. *New J. Chem.* **35**, 2551–2556 (2011).
22. Das, D. & Das, P. K. Superior activity of structurally deprived enzyme-carbon nanotube hybrids in cationic reverse micelles. *Langmuir* **25**, 4421–4428 (2009).
23. Chen, H. *et al.* Thermally responsive reversed micelles for immobilization of enzymes. *Adv. Funct. Mater.* **18**, 95–102 (2008).
24. Xie, W. L. & Ma, N. Immobilized lipase on Fe₃O₄ nanoparticles as biocatalyst for biodiesel production. *Energ. Fuel* **23**, 1347–1353 (2009).
25. Dhar, S. *et al.* Physicochemical characterization of reverse micelles of Triton X using 1-anthracene sulphonate as fluorescent probe: A spectroscopic study. *Colloid Surf. A* **349**, 117–124 (2009).
26. Gottlieb, H. E., Kotlyar, V. & Nudelman, A. NMR chemical shifts of common laboratory solvents as trace impurities. *J. Org. Chem.* **62**, 7512–7515 (1997).
27. Kumar, C. & Balasubramanian, D. Structural features of water-in-oil micro-emulsions. *J. Phys. Chem.* **84**, 1895–1899 (1980).
28. Sawada, K. & Ueda, M. Enzyme processing of wool fabrics in a non-ionic surfactant reverse micellar system. *J. Chem. Technol. Biot.* **79**, 376–380 (2004).
29. Kumar, C. & Balasubramanian, D. Spectroscopic studies on the micro-emulsions and lamellar phases of the system triton x-100 - hexanol - water in cyclohexane. *J. Colloid. Interf. Sci.* **74**, 64–70 (1980).
30. Bhardwaj, A. *et al.* Biofunctional membranes: An EPR study of active site structure and stability of papain non-covalently immobilized on the surface of modified poly(ether) sulfone membranes through the avidin-biotin linkage. *J. Membr. Sci.* **119**, 241–252 (1996).
31. Allcock, H. R. & Kwon, S. Covalent linkage of proteins to surface-modified poly(organophosphazenes) - immobilization of glucose-6-phosphate-dehydrogenase and trypsin. *Macromolecules* **19**, 1502–1508 (1986).
32. Huang, S. C., Caldwell, K. D., Lin, J. N., Wang, H. K. & Herron, J. N. Site-specific immobilization of monoclonal antibodies using spacer-mediated antibody attachment. *Langmuir* **12**, 4292–4298 (1996).
33. Vishwanath, S., Bhattacharyya, D., Huang, W. & Bachas, L. G. Site-directed and random enzyme immobilization on functionalized membranes - kinetic studies and models. *J. Membr. Sci.* **108**, 1–13 (1995).
34. Liang, Y. Y. & Zhang, L. M. Bioconjugation of papain on superparamagnetic nanoparticles decorated with carboxymethylated chitosan. *Biomacromolecules* **8**, 1480–1486 (2007).
35. Si, Y., Yan, C., Hong, F., Yu, J. & Ding, B. A general strategy for fabricating flexible magnetic silica nanofibrous membranes with multifunctionality. *Chem. Commun.* **51**, 12521–12524 (2015).
36. Si, Y., Ren, T., Li, Y., Ding, B. & Yu, J. Fabrication of magnetic polybenzoxazine-based carbon nanofibers with Fe₃O₄ inclusions with a hierarchical porous structure for water treatment. *Carbon* **50**, 5176–5185 (2012).
37. Si, Y. *et al.* *In situ* synthesis of flexible magnetic gamma-Fe₂O₃@SiO₂ nanofibrous membranes. *Nanoscale* **6**, 2102–2105 (2014).
38. Zhu, C. *et al.* Highly compressible 3D periodic graphene aerogel microlattices. *Nat. Commun.* **6**, 6962 (2015).
39. Si, Y., Ren, T., Ding, B., Yu, J. & Sun, G. Synthesis of mesoporous magnetic Fe₃O₄@carbon nanofibers utilizing *in situ* polymerized polybenzoxazine for water purification. *J. Mater. Chem.* **22**, 4619–4622 (2012).
40. Hou, H. *et al.* General strategy for fabricating thoroughly mesoporous nanofibers. *J. Am. Chem. Soc.* **136**, 16716–16719 (2014).
41. Tang, L. *et al.* Rapid adsorption of 2,4-dichlorophenoxyacetic acid by iron oxide nanoparticles-doped carboxylic ordered mesoporous carbon. *J. Colloid. Interf. Sci.* **445**, 1–8 (2015).
42. Natalello, A., Ami, D., Brocca, S., Lotti, M. & Doglia, S. M. Secondary structure, conformational stability and glycosylation of a recombinant *Candida rugosa* lipase studied by Fourier-transform infrared spectroscopy. *Biochem. J.* **385**, 511–517 (2005).
43. Zhang, N., Zang, G. L., Shi, C., Yu, H. Q. & Sheng, G. P. A novel adsorbent TEMPO-mediated oxidized cellulose nanofibrils modified with PEI: Preparation, characterization, and application for Cu(II) removal. *J. Hazard. Mater.* **316**, 11–18 (2016).
44. Fan, J. W. *et al.* Ordered mesoporous carbonaceous materials with tunable surface property for enrichment of hexachlorobenzene. *Langmuir* **32**, 9922–9929 (2016).
45. Xu, X. Q., Deng, C. H., Yang, P. Y. & Zhang, X. M. Immobilization of trypsin on superparamagnetic nanoparticles for rapid and effective proteolysis. *J. Proteome. Res.* **6**, 3849–3855 (2007).
46. Sawada, K., Ueda, M. & Kajiwara, K. Simultaneous dyeing and enzyme processing of fabrics in a non-ionic surfactant reverse micellar system. *Dyes Pigm.* **63**, 251–258 (2004).
47. Sawada, K. & Ueda, M. Adsorption behavior of direct dye on cotton in non-aqueous media. *Dyes Pigm.* **58**, 37–40 (2003).

Acknowledgements

This research was supported by National Natural Science Foundation of China (No. 21506173), Natural Science Foundation of Chongqing (No. cstc2016jcyjA0210), China Postdoctoral Science Foundation (No. 2015M582503) and Chongqing Postdoctoral Science Foundation (No. Xm2015122).

Author Contributions

S.X.Y. and Y.S. designed the research and wrote the manuscript. F.Y.D. involved the analysis of mechanical data. C.Y.Z. prepared the samples and performed SEM analysis.

Additional Information

Supplementary information accompanies this paper at doi:10.1038/s41598-017-10453-4

Competing Interests: The authors declare that they have no competing interests.

Publisher's note: Springer Nature remains neutral with regard to jurisdictional claims in published maps and institutional affiliations.



Open Access This article is licensed under a Creative Commons Attribution 4.0 International License, which permits use, sharing, adaptation, distribution and reproduction in any medium or format, as long as you give appropriate credit to the original author(s) and the source, provide a link to the Creative Commons license, and indicate if changes were made. The images or other third party material in this article are included in the article's Creative Commons license, unless indicated otherwise in a credit line to the material. If material is not included in the article's Creative Commons license and your intended use is not permitted by statutory regulation or exceeds the permitted use, you will need to obtain permission directly from the copyright holder. To view a copy of this license, visit <http://creativecommons.org/licenses/by/4.0/>.

© The Author(s) 2017